

Compositional dependence of direct transition energies in $\text{Si}_x\text{Ge}_{1-x-y}\text{Sn}_y$ alloys lattice-matched to Ge/GaAs

Phoebe M. Pearce,^{1,*} Sheau Wei Ong,² Andrew D. Johnson,³ Eng Soon Tok,² and Nicholas J. Ekins-Daukes^{1,4}

¹*Department of Physics, Imperial College London,
South Kensington, London SW7 2AZ, United Kingdom*

²*εMaGIC-Lab, Department of Physics, National University of Singapore, 2 Science Drive 3, Singapore 117551, Singapore*

³*IQE plc., Pascal Close, St. Mellons, Cardiff CF3 0LW, United Kingdom*

⁴*School of Photovoltaic and Renewable Engineering,
University of New South Wales, Sydney, New South Wales 2052, Australia*

(Dated: March 17, 2022)

$\text{Si}_x\text{Ge}_{1-x-y}\text{Sn}_y$ ternary alloys are a candidate material system for use in solar cells and other optoelectronic devices. We report on the direct transition energies and structural properties of Ge-rich $\text{Si}_x\text{Ge}_{1-x-y}\text{Sn}_y$ alloys with six different compositions up to 10% Si and 3% Sn, lattice-matched to Ge or GaAs substrates. The direct transitions occurring between 0.9 and 5.0 eV were investigated using spectroscopic ellipsometry (SE), and the resulting data was used to obtain the dielectric functions of the $\text{Si}_x\text{Ge}_{1-x-y}\text{Sn}_y$ layer by fitting a multi-layer model. Values for the E_0 , E_1 , Δ_1 , E'_0 and E_2 transition energies were then found by differentiating these dielectric functions to extract the locations of critical points. Structurally, the composition of the samples was measured using energy-dispersive X-ray measurements (EDX). The lattice constants predicted from these compositions are in good agreement with reciprocal space maps obtained through X-ray diffraction (XRD). The results confirm that a 1 eV direct absorption edge can be achieved using relatively low Si and Sn fractions ($< 10\%$ and $< 3\%$ respectively), while the higher-energy critical points show smaller shifts relative to Ge and match results previously observed or predicted in the literature.

I. INTRODUCTION

$\text{Si}_x\text{Ge}_{1-x-y}\text{Sn}_y$ ternary alloys have been a topic of research interest for a variety of applications, including group IV lasers [1, 2], photodiodes [3], light-emitting diodes (LEDs) [4, 5] and photovoltaics [4, 6–8]. By controlling the alloy composition, it is possible to tune the bandgap, higher-energy interband transitions, and the lattice constant. For photovoltaic applications, semiconductors with an absorption edge around 1 eV are an area of current research interest for current-matched in multi-junction solar cells using well-established material systems such as Ge, GaAs and $\text{In}_{0.5}\text{Ga}_{0.5}\text{P}$. However, identifying materials which can be grown with sufficiently high material quality at the required bandgap and lattice constant is a challenge. $\text{Si}_x\text{Ge}_{1-x-y}\text{Sn}_y$ can be engineered to have the same lattice constant as Ge but a higher bandgap and is therefore a suitable candidate material for these applications.

$\text{Si}_x\text{Ge}_{1-x-y}\text{Sn}_y$ alloys with a direct absorption edge around 1 eV have a high atomic fraction of Ge ($x > 85\%$) and an atomic Si:Sn ratio of around 3.7:1, necessary to maintain the desired lattice constant according to Vegard's law [9]. The addition of Si to Ge increases the energy of both the fundamental bandgap (0.67 eV in pure Ge [10]) and the lowest-energy direct transition (0.80 eV in pure Ge [10]) but will reduce the lattice

constant as Si has a smaller atomic radius than Ge. Conversely, the addition of Sn increases the lattice constant and reduces the fundamental bandgap. By balancing the relative amounts of Si and Sn in the alloy, it is possible to engineer a material which has a higher bandgap and absorption edge than Ge but the same lattice constant, although this material is expected to retain an indirect bandgap lower in energy than the 1 eV transition; it is not possible to achieve a 1 eV direct fundamental bandgap [11, 12]. We have previously reported on the near-bandgap behaviour of $\text{Si}_x\text{Ge}_{1-x-y}\text{Sn}_y$ alloys, investigating both the indirect fundamental bandgap and the circa-1 eV direct transition through spectroscopic measurements and theoretical calculations [12]. Here, we confirm the circa-1 eV direct absorption edge and investigate the higher-energy interband transitions for the same set of samples.

High-quality $\text{Si}_x\text{Ge}_{1-x-y}\text{Sn}_y$ alloys have been grown mainly, and most successfully, through chemical vapour deposition (CVD) and molecular beam epitaxy (MBE) [13]. Ultra-high vacuum CVD (UHV-CVD) growth of $\text{Si}_x\text{Ge}_{1-x-y}\text{Sn}_y$ was first reported by Bauer et al. [14], followed by the first reports of photoluminescence signal from $\text{Si}_x\text{Ge}_{1-x-y}\text{Sn}_y$ by Soref et al. [15]. These samples were grown using deuterated tin (SnD_4); this precursor was also used in the fabrication of the most successful demonstration to date of a multi-junction cell with a $\text{Si}_x\text{Ge}_{1-x-y}\text{Sn}_y$ sub-cell [8]. $\text{Si}_x\text{Ge}_{1-x-y}\text{Sn}_y$ has also been grown through both reduced-pressure CVD, using the commercially available precursor SnCl_4 , [16–18] and MBE [19–21]. This development of $\text{Si}_x\text{Ge}_{1-x-y}\text{Sn}_y$ epitaxy has happened in conjunction with the epitaxy of direct-bandgap GeSn alloys for laser applications, mostly

*Electronic address: p.pearce@unsw.edu.au; Present address: School of Photovoltaic and Renewable Energy Engineering, University of New South Wales, Sydney, NSW, Australia

in heterostructures containing (Si)GeSn. For research applications, custom-built epitaxy reactors or highly-customized commercial reactors are often used, in combination with different precursors for Si and Ge depending on the composition being grown [22]. In addition to SnD_4 , silicon and more complex germanium hydrides ($\text{Ge}_n\text{H}_{2n+2}$ and $\text{Si}_n\text{H}_{2n+2}$) with $n > 1$ are commonly used, which are more expensive than the common commercial precursors. The samples investigated here were grown using a commercial CVD reactor and precursor materials, with the aim of developing a $\text{Si}_x\text{Ge}_{1-x-y}\text{Sn}_y$ growth process which reduces the complexity and cost associated with multi-junction cell growth. To study the direct inter-band transitions which dominate the dielectric function of these materials, spectroscopic ellipsometry was performed over the wavelength range 250–1800 nm (0.69–4.96 eV). The composition of the samples was measured through energy-dispersive X-ray spectroscopy (EDX) using a scanning electron microscope (SEM) while structural features were studied using X-ray diffraction (XRD) and optical microscopy. These results confirm that with these growth methods, it is possible to fabricate material with a 1 eV absorption edge, significantly blueshifted from pure Ge, on Ge or GaAs substrates, providing an important step towards successfully fabricating a multi-junction cell incorporating $\text{Si}_x\text{Ge}_{1-x-y}\text{Sn}_y$.

II. METHODS

A. Sample growth

$\text{Si}_x\text{Ge}_{1-x-y}\text{Sn}_y$ samples were grown through low-pressure CVD (chemical vapour deposition) in an ASM Epsilon 2000 CVD epitaxy reactor. Germane (GeH_4), disilane (Si_2H_6) and tin chloride (SnCl_4) precursors were used, with H_2 as the carrier gas. Two sets of samples across the composition range are considered here: one set grown on GaAs substrates with a thin (≈ 60 nm) Ge seed layer, which will be referred to as Set A, and one set grown on Ge substrates which were overgrown with approximately 500 nm of lattice-matched $\text{In}_{0.012}\text{Ga}_{0.988}\text{As}$ grown through metal-organic vapour-phase epitaxy (MOVPE), referred to as Set B. The layer structure of the samples is shown in Fig. 1. Samples within both of these sets were grown at three different compositions, all aiming for an approximately 3.7:1 ratio of Si:Sn to achieve the same lattice constant as Ge, assuming the lattice constant of the alloy obeys Vegard's law [9, 23]. For Set B, two different $\text{Si}_x\text{Ge}_{1-x-y}\text{Sn}_y$ thicknesses were grown for each composition, giving a total of three samples in Set A and six samples in Set B. The resulting sample structures, compositions, layer thicknesses and the labels used for the samples are summarized in Table I.

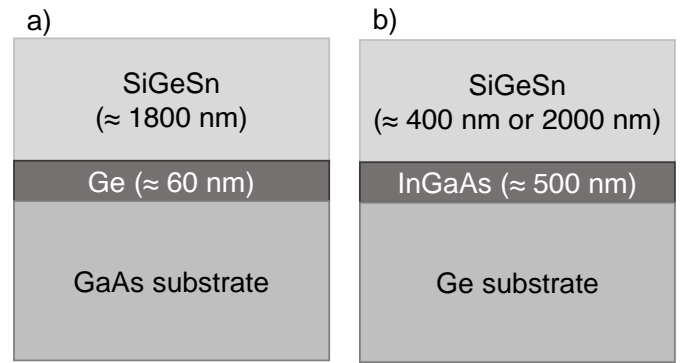


FIG. 1: Schematic of the layer structure of the epitaxial $\text{Si}_x\text{Ge}_{1-x-y}\text{Sn}_y$ samples. From [12].

B. Structural characterization

The samples' surface morphology was examined by taking optical images using an Olympus BX51 Microscope equipped with polarizer, rotatable analyzer and Nomarski prism taken at $100\times$ magnification. Compositions were obtained from energy dispersive X-ray measurements (EDX) performed using a JEOL JSM-6700F Field-emission Scanning Electron microscope equipped with Oxford instruments X-Max 150 mm^2 taken at an accelerating voltage of 15 kV. The sample composition was measured at 10 points on the surface of each sample (averages and standard deviations are reported in Table I); measurements of the same samples during different measurement sessions showed these results to be repeatable. The crystalline quality and lattice constant of the samples was investigated using a Malvern-Panalytical Empyrean X-ray diffractometer by measuring the symmetrical (004) and asymmetrical (224) rocking curves and reciprocal space maps (RSMs).

C. Spectroscopic ellipsometry

Spectroscopic ellipsometry (SE) measurements were performed using a J. A. Woollam Co. VASE ellipsometer over a spectral range of 250-1800 nm at angles 75, 77 and 79°. Ellipsometry measures the ratio of the complex reflection amplitudes r_s and r_p for incident polarized light, and the data is usually expressed in terms of the angles Ψ and Δ :

$$\rho = \frac{r_p}{r_s} = \tan \Psi \cdot e^{i\Delta} \quad (1)$$

Ψ quantifies the magnitude of the ratio and lies in the range $0 - 90^\circ$, while Δ determines the phase and lies in the range $0 - 180^\circ$.

For a sample with multiple layers, it is generally necessary to fit a multi-layer model to the data which accounts for reflection at the front surface and each inter-

TABLE I: $\text{Si}_x\text{Ge}_{1-x-y}\text{Sn}_y$ thickness (from fits to SE data) d_{SiGeSn} , composition of the $\text{Si}_x\text{Ge}_{1-x-y}\text{Sn}_y$ measured through SEM-EDX, and resulting lattice constant obtained via Vegard's law. The samples are labelled numerically within sets in order of increasing Si/Sn composition. The composition values are the mean across ten measurements of each sample (the values in brackets are the standard deviation). The relaxed $\text{Si}_x\text{Ge}_{1-x-y}\text{Sn}_y$ lattice constant a_{SiGeSn} is calculated according to Vegard's law [9] based on the compositions (the uncertainty is due to the error carried forward from the composition measurements).

Sample	d_{SiGeSn} (nm)	Si (atomic %)	Sn (atomic %)	a_{SiGeSn} (Å)
A1	1768	4.6 (0.2)	0.9 (0.1)	5.65(4)
A2	1851	6.8 (0.5)	1.6 (0.1)	5.65(5)
A3	1906	9.6 (0.4)	2.2 (0.1)	5.65(4)
B1 (thin)	335	n.m.	n.m.	5.65(8)
B2 (thin)	367	n.m.	n.m.	5.65(7)
B3 (thin)	365	n.m.	n.m.	5.65(7)
B1 (thick)	2036	2.6 (0.3)	0.8 (0.2)	5.65(8)
B2 (thick)	2115	5.9 (0.2)	1.5 (0.1)	5.65(7)
B3 (thick)	2080	8.4 (0.2)	2.5 (0.1)	5.65(7)

face, and the resulting interference at each wavelength; such interference is evident in the data shown in Fig. 4. A parametric Herzinger-Johs [24] model was used to fit the $\text{Si}_x\text{Ge}_{1-x-y}\text{Sn}_y$ optical constants. Such a parametric model has the advantages of reducing the number of fitting parameters (compared to fitting the ε_1 and ε_2 values point-by-point) and enforcing Kramers-Kronig consistency [24, 25], while increasing the flexibility of the peak shapes compared to a more physically-constrained model such as a Critical Point Parabolic Band (CPPB) model [26]. The drawback compared to a CPPB model is that due to the flexible peak shape, the fitting parameters drawn from a parametric model are not necessarily physically meaningful; e.g. the centre energy of a peak may not correspond directly to a specific transition energy in the material's band structure. For this reason, rather than taking the desired transition energies directly from the obtained fitting parameters, the dielectric function obtained for the $\text{Si}_x\text{Ge}_{1-x-y}\text{Sn}_y$ was differentiated in order to obtain the relevant centre energies, as described below.

The structure of the different sample types, used as a starting point for these models, is shown in Fig. 1, comprising the Ge or GaAs substrate, the InGaAs layer (in the case of the Set B samples), and the $\text{Si}_x\text{Ge}_{1-x-y}\text{Sn}_y$ layer. A GeO_2 surface layer [27] was also included in the fits; the inclusion of a thin surface layer (fitted as 1-2 nm thick for all the $\text{Si}_x\text{Ge}_{1-x-y}\text{Sn}_y$ samples) is necessary to achieve a good fit to the data, including for a reference measurement of a Ge substrate. GeO_2 was used since the samples are mostly Ge, so it was assumed the surface oxide is mostly Ge-based. A similar method to the fitting procedure for the $\text{Si}_x\text{Ge}_{1-x-y}\text{Sn}_y$ optical constants outlined in [28] was used. The starting points for the layer thicknesses were the nominal thicknesses targeted during CVD growth. Initially, the $\text{Si}_x\text{Ge}_{1-x-y}\text{Sn}_y$ layer was assumed to be pure Ge; since we are considering Ge-heavy (> 85%) samples of $\text{Si}_x\text{Ge}_{1-x-y}\text{Sn}_y$, using the well-known optical constants of Ge as a placeholder for $\text{Si}_x\text{Ge}_{1-x-y}\text{Sn}_y$ gives a good starting point for fitting the layer thicknesses. For the Set B samples, the InGaAs buffer layer thickness was also allowed to

vary at this stage; in each case the deviation from the nominal thickness of 500 nm was found to be ≤ 10 nm. The starting point for the Herzinger-Johs model fits for $\text{Si}_x\text{Ge}_{1-x-y}\text{Sn}_y$ was the built-in model for Ge [25]. The model allows for very flexible peak shapes; each feature is described by seven variable parameters which control the peak's strength, centre energy, and broadening, with further parameters controlling the shape and asymmetry of the peak. Here, only the peak strength (A), centre energy (E_0) and broadening (B) were fitted, with the other parameters kept fixed at the Ge values. This was to avoid unreasonable peak shapes, including some with discontinuities in the dielectric function, especially in the low-energy region where thin-film interference and noise due to signal depolarization affects the SE measurements[39]. It was found that excellent fits to the data could be achieved without varying the other peak shape parameters. The parameters for the $\text{Si}_x\text{Ge}_{1-x-y}\text{Sn}_y$ optical constants were fitted starting at high energies, initially fitting only the centre energies of the peak followed by allowing the peak strength and broadening to vary. The layer thickness of the $\text{Si}_x\text{Ge}_{1-x-y}\text{Sn}_y$ is allowed to continue to vary while the optical constants are fitted. The data measured at all the incidence angles (75, 77 and 79°) are fitted simultaneously. The optical constants for the other layers (InGaAs, Ge and GaAs) came from the WVASE software database, except for those of GeO_2 which were defined according to a Sellmeier model using parameters from [27].

After the layer thicknesses have been determined exactly, and a parametric model for the $\text{Si}_x\text{Ge}_{1-x-y}\text{Sn}_y$ optical constants has been fitted, a point-by-point fit where ε_1 and ε_2 are fitted separately at each measurement wavelength is also performed, keeping the layer thicknesses fixed. The two fitting methods agree very well for energies above ≈ 1 eV (depending on the $\text{Si}_x\text{Ge}_{1-x-y}\text{Sn}_y$ composition). Below these energies (i.e. below the lowest direct transition in the $\text{Si}_x\text{Ge}_{1-x-y}\text{Sn}_y$, where $\text{Si}_x\text{Ge}_{1-x-y}\text{Sn}_y$ is only very weakly absorbing) the presence of thin-film interference fringes in the data significantly affects the point-by-point fits, as shown in the Supplemental Information [29].

The fundamental indirect gap – 0.67 eV for Ge at room temperature and blueshifted to 0.7–0.8 eV for the $\text{Si}_x\text{Ge}_{1-x-y}\text{Sn}_y$ samples, as determined by photoluminescence measurements [12]) – is not included in the Herzinger-Johs model. Even considering the expected blueshift in this bandgap relative to Ge for the $\text{Si}_x\text{Ge}_{1-x-y}\text{Sn}_y$ samples, this transition occurs very close to or beyond the longest wavelength which can be measured using the V-VASE ellipsometer, and is expected to contribute so weakly to the dielectric function that it would be extremely difficult to observe through ellipsometry. This transition was investigated through photoluminescence measurements of the same set of samples as reported in [12].

D. Critical point fits

The optical constants obtained from the SE data were differentiated twice to obtain fits for the centre energies of the peaks identified as corresponding to the E_0 , E_1 , $E_1 + \Delta_1$, E'_0 and E_2 transition energies, using a method similar to [30]. The critical points observed in the second derivative of the dielectric function were fitted to expressions of the form:

$$\frac{d^2(E^2\varepsilon)}{dE^2} = \frac{A_i e^{i\Phi_i}}{(E - E_i + i\Gamma_i)^m} \quad (2)$$

where the strength parameter A_i , phase Φ_i , centre energy E_i and broadening term Γ_i are fitting parameters. The exponent m is fixed and depends on the type of critical point (CP) being fitted. The E_0 and $E_0 + \Delta_0$ features were fitted as a 3D M0 type CPs with the exponent $m = 3/2$, while the higher-energy CPs were fitted as 2D M1 type CPs with $m = 2$. The choice of this differential (specifically the choice to differentiate the quantity $E^2\varepsilon$ rather than the more common choice of simply differentiating ε), and how the differentiation was performed computationally, are discussed in the Supplemental Material [29].

As described above, the point-by-point fit was reliable above ≈ 1 eV, while below these energies it was very noisy due to the interference fringes in the measurement and signal depolarization. Thus, for the analysis of ellipsometric data presented in Section III C, the point-by-point fits were used for energies > 1.5 eV to fit the E_1 , $E_1 + \Delta_1$, E'_0 and E_2 centre energies while the Herzinger-Johs parametric model fit was used to obtain E_0 .

III. RESULTS

A. Structural measurements

The composition and lattice constant of the $\text{Si}_x\text{Ge}_{1-x-y}\text{Sn}_y$ samples were characterized using

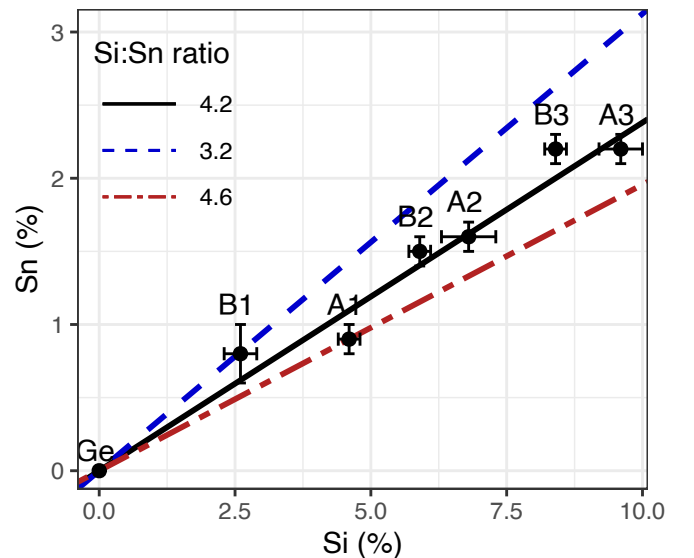


FIG. 2: The Si:Sn ratio for each of the samples with composition measured through SEM-EDX. For Set B, only the thicker samples were measured. The error bars show the standard deviation from ten measurements of the same sample.

SEM-EDX and XRD (rocking curve and reciprocal space mapping) measurements, clearly showing the increasing Si and Sn compositions within the sample sets. Table I gives the composition obtained through EDX measurements, and the predicted lattice constant through Vegard’s law. Fig 2 shows the Si and Sn fractions of each sample; all samples lie between a 4.6:1 and 3.2:1 Si:Sn ratio, with the Set B samples having a lower ratio than the Set A samples, meaning the Set B samples are more closely lattice-matched to their Ge substrates, while the Set A samples are more closely lattice-matched to their GaAs substrates. For all the samples, the thickness of the epitaxial $\text{Si}_x\text{Ge}_{1-x-y}\text{Sn}_y$ layer is expected to be below the critical thickness, as shown in the Supplemental Material [29].

Surface imaging shows the presence of defects, but no cross-hatching or features which indicate relaxation of the epitaxial layer. For Set B, only the thicker samples (≈ 2000 nm) were measured in these structural measurements, and it was assumed that the corresponding thinner (≈ 400 nm) $\text{Si}_x\text{Ge}_{1-x-y}\text{Sn}_y$ layers have very similar compositions; this is corroborated by the consistency of the dielectric function across the different thicknesses, as discussed in the next section. The surfaces of both sets of samples show ‘bubble’ and ‘pyramid’-like defects, as shown in Fig. 3(a)-(c). Given the known difficulties of $\text{Si}_x\text{Ge}_{1-x-y}\text{Sn}_y$ growth, especially regarding Sn incorporation, it is reasonable to assume these defects may be related to segregation of Sn during growth; however, additional EDX measurements comparing flat areas of the surface with the defect features do not indicate a measurably different composition within either of these feature

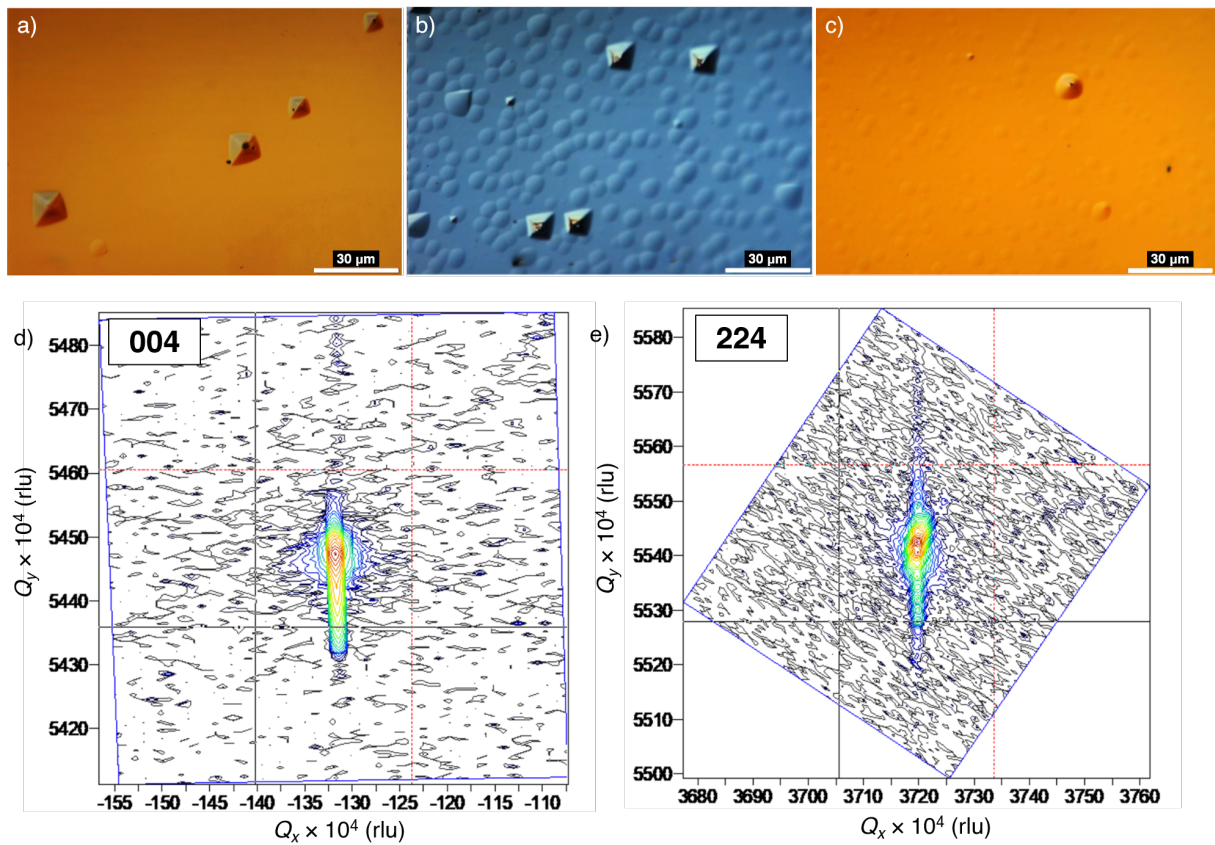


FIG. 3: (a)-(c) Optical microscopy image of the surface of samples A1, A2 and A3 respectively, taken at $100\times$ magnification. (d) RSM measured around the (004) direction for sample A1. (e) RSM measured around the (224) direction for sample A1.

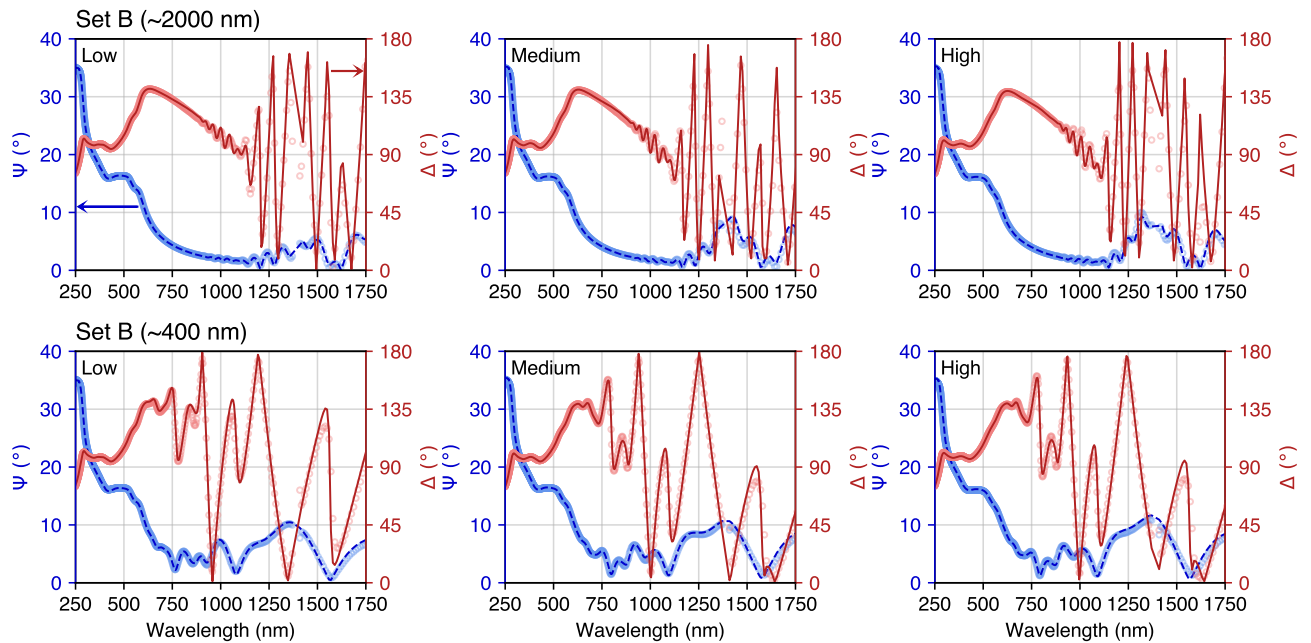


FIG. 4: Ellipsometric angles Ψ (left axis, in blue) and Δ (right axis, in red) for the Set B samples, as measured (open circles) with light incident at 77° and as calculated through the fitted multi-layer model (lines). The top row shows the results for the thicker samples in order of increasing Si/Sn composition, while the bottom row shows the results for the thinner samples. The $\text{Si}_x\text{Ge}_{1-x-y}\text{Sn}_y$ layer thicknesses fitted in each case are given in Table I.

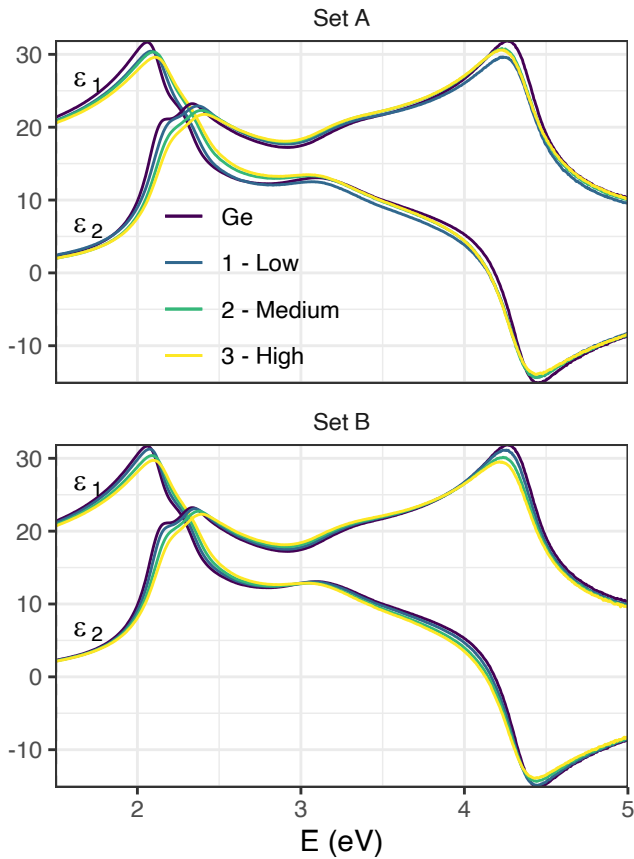


FIG. 5: Real (ϵ_1) and imaginary (ϵ_2) parts of the dielectric function of the $\text{Si}_x\text{Ge}_{1-x}\text{Sn}_y$ samples, obtained through fitting the ellipsometry data.

types. The pyramid-type defects penetrate into the bulk of the material significantly, and appear to be the results of growth along a different crystal axis to the bulk film, although further investigation is required.

Rocking curves and reciprocal space maps (RSMs) were measured around the (004) and (224) lattice points. Fig. 3(d) and (e) show the RSM scans for sample A1; RSM data for the other Set A samples around both points is given in the Supplemental Material [29]. Only the out-of-plane lattice constant can be observed in the (004) scans, while the asymmetric (224) scan will contain contributions from both the in-plane and out-of-plane lattice constants. For samples A1 and A3, some spread around a single RSM peak is observed in both the (004) and (224) RSMs, but only a single clearly-defined peak is visible, indicating that the epi-layer is very closely lattice-matched to the substrate. The peak broadening in reciprocal space at constant Q_x also indicates pseudomorphic (constant lattice constant) growth, with the in-plane lattice parameter strained to the substrate (GaAs) lattice constant. For sample A2, a clear split in the peak in the (004) RSM is observed, showing that the epi-layer has a different out-of-plane lattice constant than the substrate. This indicates the presence of biaxial strain and thus that

the epitaxial layer has not relaxed. The XRD peaks for this sample correspond to lattice constants of 5.6537 Å and 5.6567 Å, with the former value being the GaAs lattice constant. This indicates that the relaxed lattice constant of sample A2 is larger than that of GaAs, causing in-plane compressive strain in the $\text{Si}_x\text{Ge}_{1-x}\text{Sn}_y$ and expansion of the out-of-plane lattice constant. Assuming the in-plane lattice constant is pinned to that of GaAs, as indicated by the RSM in the (224) direction, and taking the Poisson ratio [40] of the $\text{Si}_x\text{Ge}_{1-x}\text{Sn}_y$ to be 0.3 (a typical value used for Ge [31]), the relaxed lattice constant is calculated to be 5.6553 Å, in excellent agreement with the value of 5.655 Å calculated through Vegard's law using the composition measurements from SEM-EDX (see Table I). Sample A2 was the Set A sample with the largest predicted deviation from the GaAs lattice constant through Vegard's law, and the only sample for which a clear second peak in the RSM can be observed. This indicates that the samples are closely lattice-matched to the substrates, with some strain, and the SEM-EDX composition measurements and XRD give consistent results.

B. Ellipsometry

The ellipsometry data for the Set B samples, and the result of the model fit, are shown in Fig. 4 (data for the Set A samples is shown in the Supplemental Material [29], and the SE data and resulting fits of the $\text{Si}_x\text{Ge}_{1-x}\text{Sn}_y$ optical constants are available [32]). This data shows clear effects due to thin-film interference in the $\text{Si}_x\text{Ge}_{1-x}\text{Sn}_y$ layer; while the higher-energy transitions (2 eV and above) are clearly visible in the raw data, the near-bandgap data is dominated by interference fringes which depend on the thickness of the $\text{Si}_x\text{Ge}_{1-x}\text{Sn}_y$ layer. This can be seen clearly by comparing the data in Fig. 4 from the samples with the same composition but different thicknesses, with the thinner samples showing much wider interference fringes.

For the Set B samples, the optical constants of the $\text{Si}_x\text{Ge}_{1-x}\text{Sn}_y$ were obtained only through fitting to the data from the thicker samples. To fit the SE data of the thinner samples, only the layer thicknesses were allowed to vary. This allowed for a validation of the optical constants fitted and a check that the $\text{Si}_x\text{Ge}_{1-x}\text{Sn}_y$ layer has the same composition for the different thicknesses; the models for the thinner Set B samples show excellent agreement with the data despite only the layer thicknesses being fitted as shown in Fig. 4. Fig. 5 shows the dielectric function fitted for each $\text{Si}_x\text{Ge}_{1-x}\text{Sn}_y$ composition in Set A and Set B, showing how the absorption edge and lower-energy critical points (< 2.5 eV) blueshift with increasing Si/Sn composition while the higher-energy critical points redshift. Fig. 6 shows the real and imaginary part of the dielectric function fitted to the $\text{Si}_x\text{Ge}_{1-x}\text{Sn}_y$ layers of the Set A samples, and their first and second derivatives. Through fitting equa-

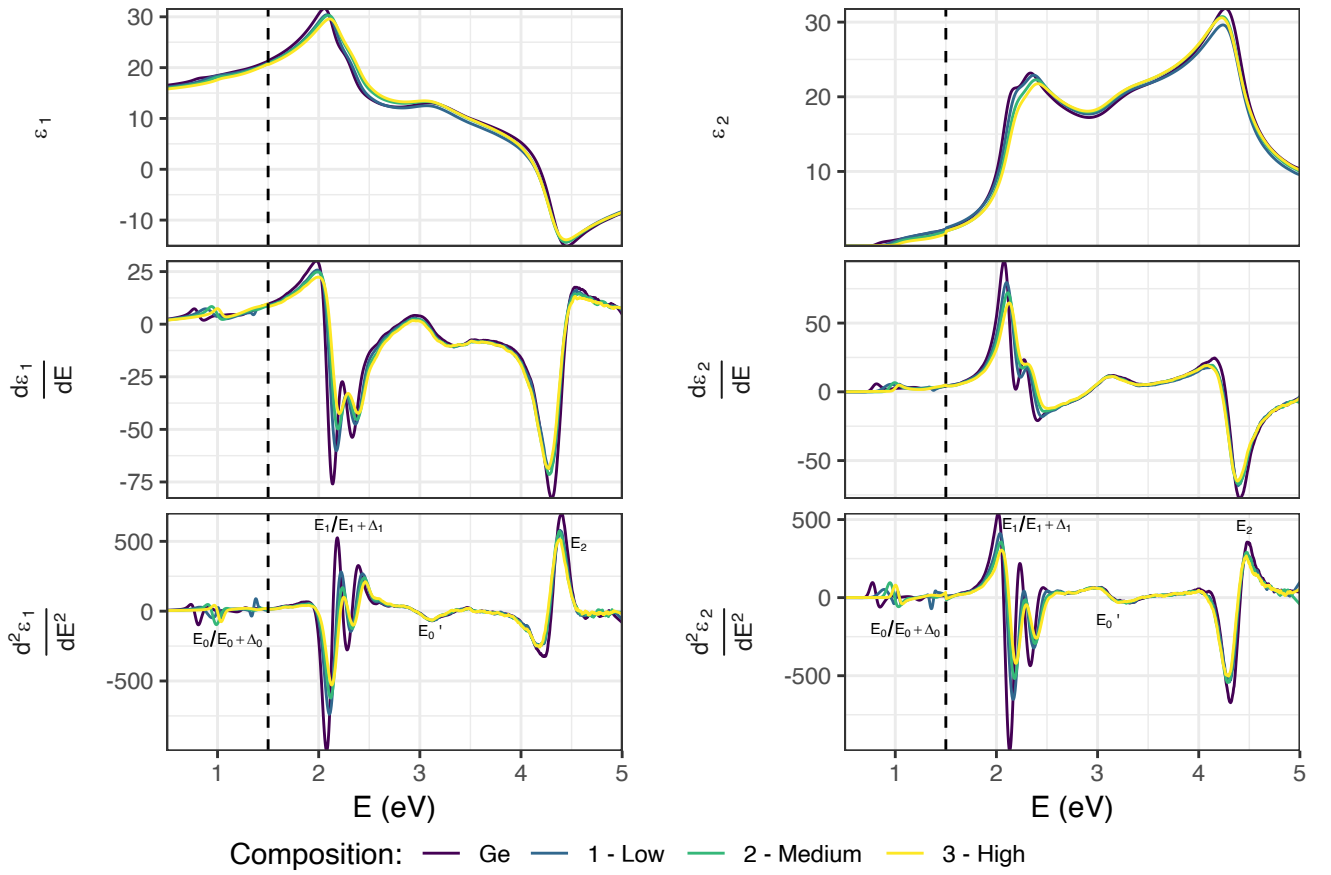


FIG. 6: Real (ε_1) and imaginary (ε_2) parts of the dielectric functions from fits to ellipsometry data for sample set A, and their first and second derivatives with respect to energy. Data for a Ge substrate is shown for reference in each plot. Data below 1.5 eV is from the parametric model fit, while data above 1.5 eV is from a point-by-point fit to the data; the dashed line indicates where the data is stitched together.

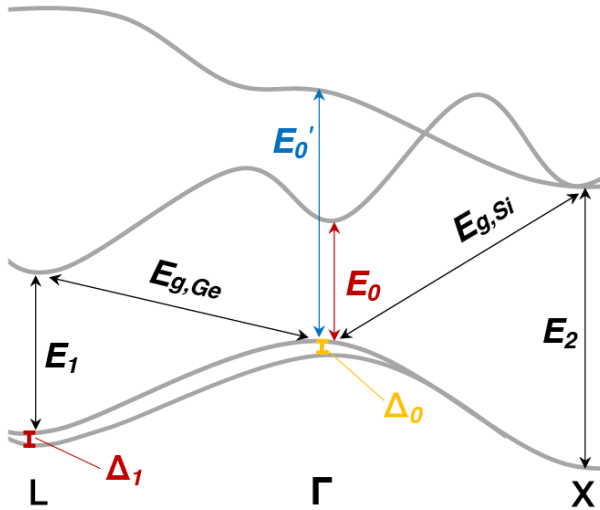


FIG. 7: Simplified band structure of $\text{Si}_x\text{Ge}_{1-x-y}\text{Sn}_y$ showing key indirect and direct transition energies in the band structure.

tion 2, the exact location of the transition energies can be extracted from these derivatives; these sharp features are clearly visible in the second derivative shown in Fig. 6.

C. Critical point fitting

Fig. 7 shows a simplified version of the $\text{Si}_x\text{Ge}_{1-x-y}\text{Sn}_y$ band structure, indicating the point in the band structure at which the transitions discussed in this section take place. Fig. 8 shows the critical point fits according to equation 2 (with $m = 3/2$ for a E_0 and $m = 2$ for all the other features) for the E_0 , $E_1/E_1 + \Delta_1$, E_0' and E_2 features obtained from differentiating the dielectric functions shown in Fig. 5. For each transition, the phase was fixed to be the same across compositions, choosing the phase which gives the best fit across all the samples (see Supplemental Material Table S1 for full fitting results [29]). For E_0 , the parametric model fits were differentiated twice, while to fit the higher-energy critical points the point-by-point dielectric constant fit was used. The

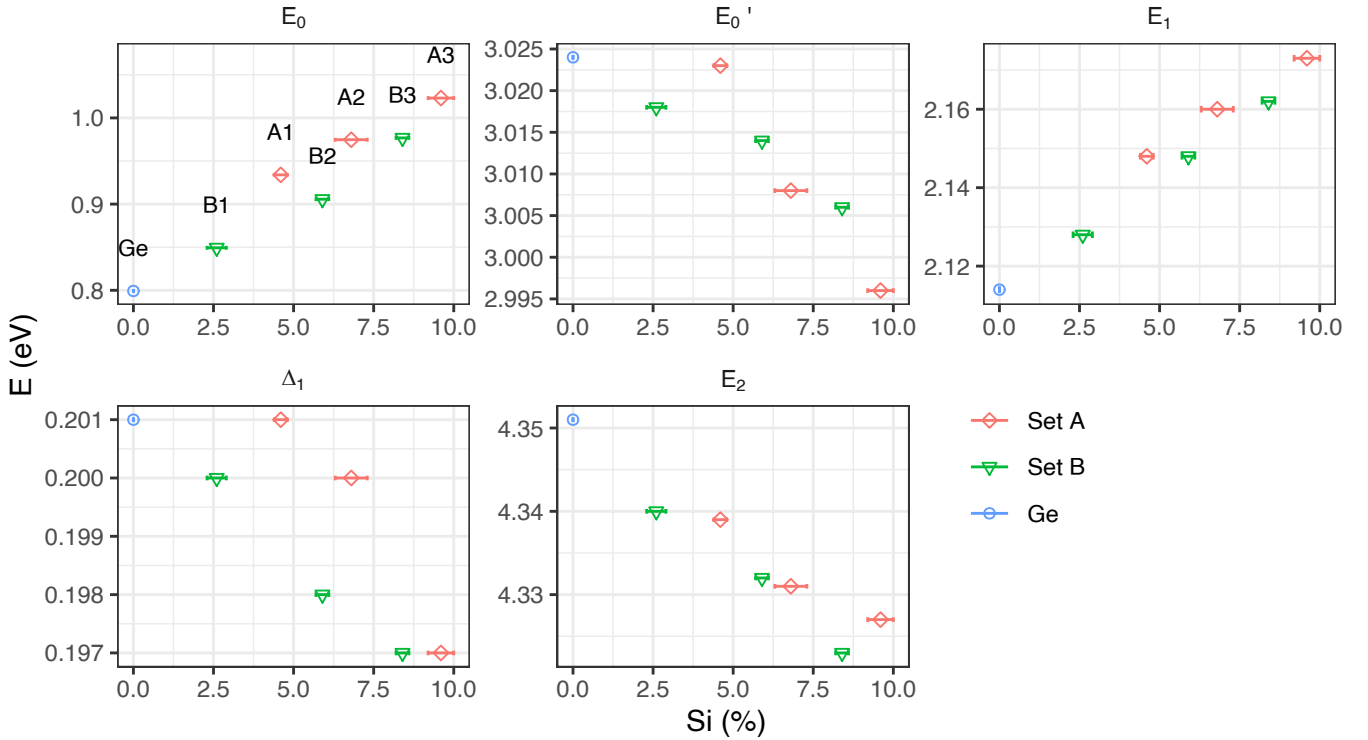


FIG. 9: Summary of centre energies for the different direct transitions extracted from SE data.

TABLE II: Summary of centre energies fitted to the $\text{Si}_x\text{Ge}_{1-x-y}\text{Sn}_y$ and Ge critical points as obtained through SE measurements. All values are in eV.

Comp.	E_0	E_1	$E_1 + \Delta_1$	E_0'	E_2
Ge	0.799	2.114	2.315	3.024	4.351
A1	0.934	2.148	2.349	3.011	4.339
A2	0.975	2.160	2.360	3.008	4.331
A3	1.023	2.173	2.370	3.002	4.327
B1	0.849	2.128	2.328	3.016	4.340
B2	0.906	2.148	2.346	3.007	4.332
B3	0.977	2.162	2.359	2.999	4.323

blueshift than the Set A samples, as can be seen in Fig. 9. The E_1 and $E_1 + \Delta_1$ energies, around 2.2 and 2.3 eV respectively, also blueshift with increased Si/Sn composition as expected [22, 33]. Meanwhile, E_0' and E_2 redshift very slightly (Fig. 9), each by less than 30 meV between Ge and the highest-composition sample (A3), as does the split-off energy Δ_1 though by only 4 meV. The reduction in E_0' matches previously reported results [22]. Although different sources report different values for the E_0' energies of Ge and Si [10], the values for Si are generally slightly higher by around 0.2 eV, yet we observe a slight redshift here; this could be due to the presence of α -Sn (which has a lower E_0 by ≈ 1 eV) outweighing the effect of the Si, or because what is treated here as a single transition is in fact made up of at least two contributing critical points. This can be seen at the

high-energy edge of Fig. 8(c), where there appears to be a second weaker feature visible around 3.4-3.5 eV. The reduction in E_2 is also consistent with previous literature results [22, 34], and expected from the lower E_2 energy of both Si and α -Sn compared to Ge. Note that values of Δ_0 were not fitted to the ellipsometry data; this contribution is relatively much weaker than that of E_0 , which is already much weaker than the higher-energy transitions. It was not possible to obtain a reliable, unique fit to the $E_0 + \Delta_0$ critical point, so it was excluded from the second-derivative fits. Photoreflectance measurements of the same samples indicate that Δ_0 stays almost constant [12].

IV. CONCLUSIONS

$\text{Si}_x\text{Ge}_{1-x-y}\text{Sn}_y$ is a promising candidate material for solar cells and other optoelectronic applications, with previous experimental and theoretical results indicating that a direct transition energy at 1 eV can be achieved at atomic compositions $< 10\%$ Si and $< 3\%$ Sn, with the resulting alloy being lattice-matched to Ge or GaAs. The results of ellipsometry measurements presented here confirm this, showing E_0 energies between 0.98 and 1.02 eV for alloys with compositions of 6.8-9.6% Si and 1.6-2.5% Sn. The higher-energy (up to 5 eV) direct transitions at the Γ , X and L points in the bandstructure were also investigated, showing a blueshift in E_1 and small redshifts

in Δ_1 , E'_0 and E_2 , in good agreement with previously-published results.

At these compositions, $\text{Si}_x\text{Ge}_{1-x-y}\text{Sn}_y$ retains a fundamentally indirect “Ge-like” bandgap. This indirect transition was studied for this set of samples using photoluminescence, showing bandgaps in the range 0.7-0.75 eV [12]. While this lower-lying indirect transition is expected to affect the voltage of a solar cell adversely, $\text{Si}_x\text{Ge}_{1-x-y}\text{Sn}_y$ will have a higher fundamental bandgap and thus voltage than Ge (if used instead of Ge in e.g. a triple-junction device with InGaP and (In)GaAs). In a four-junction InGaP/(In)GaAs/SiGeSn/Ge device, where current-matching is important, absorption across the $\text{Si}_x\text{Ge}_{1-x-y}\text{Sn}_y$ will be dominated by the direct edge and the additional $\text{Si}_x\text{Ge}_{1-x-y}\text{Sn}_y$ junction will still provide a voltage boost compared to the standard triple-junction architecture. Thus, the 1 eV direct absorption edge is still expected to provide benefits in terms of current-matching, and the higher indirect gap compared

to Ge can provide an increase in voltage.

Data access

The spectroscopic ellipsometry data associated with this work are openly available, and can be accessed via Ref. 32.

Acknowledgements

This work was supported by the Engineering and Physical Sciences Research Council, U.K. (EPSRC; via a CASE Studentship, held by P.P. and sponsored by IQE plc.), and by the Royal Society (via an Industry Fellowship, held by N.J.E-D.).

-
- [1] G. Sun, R. A. Soref, and H. H. Cheng, *Journal of Applied Physics* **108** (2010), ISSN 00218979.
- [2] Y. Zhou, J. Margetis, G. Abernathy, W. Dou, P. C. Grant, B. Alharthi, W. Du, A. Wadsworth, Q. Guo, H. Tran, et al., 2019 Conference on Lasers and Electro-Optics, CLEO 2019 - Proceedings **1**, 2019 (2019).
- [3] R. T. Beeler, D. J. Smith, J. Kouvetakis, and J. Menéndez, *IEEE Journal of Photovoltaics* **2**, 434 (2012), ISSN 21563381.
- [4] R. T. Beeler, J. Gallagher, C. Xu, L. Jiang, C. L. Senaratne, D. J. Smith, J. Menendez, A. V. G. Chizmeshya, and J. Kouvetakis, *ECS Journal of Solid State Science and Technology* **2**, Q172 (2013), ISSN 2162-8769, URL <http://jss.ecsdl.org/cgi/doi/10.1149/2.034309jss>.
- [5] N. von den Driesch, D. Stange, S. Wirths, D. Rainko, I. Povstugar, A. Savenko, U. Breuer, R. Geiger, H. Sigg, Z. Ikonc, et al., *Small* **13**, 1603321 (2017), ISSN 16136810, URL <http://doi.wiley.com/10.1002/sml1.201603321>.
- [6] Y.-y. Fang, J. Xie, J. Tolle, R. Roucka, V. R. D’Costa, A. V. G. Chizmeshya, J. Menendez, and J. Kouvetakis, *Journal of the American Chemical Society* **130**, 16095 (2008), ISSN 0002-7863, URL <http://pubs.acs.org/doi/abs/10.1021/ja806636c>.
- [7] C. I. Ventura, J. D. Querales Flores, J. D. Fuhr, and R. A. Barrio, *Progress in Photovoltaics: Research and Applications* **23**, 112 (2015), ISSN 10627995, 1303.4604, URL <http://dx.doi.org/10.1002/pip.1160><http://doi.wiley.com/10.1002/pip.1160>
- [8] R. Roucka, A. Clark, T. Wilson, T. Thomas, M. Führer, N. Ekins-Daukes, A. Johnson, R. Hoffman, and D. Begarney, *IEEE Journal of Photovoltaics* **6**, 1025 (2016), ISSN 21563381.
- [9] L. Vegard, *Zeitschrift für Physik* **5**, 17 (1921), ISSN 1434-6001, URL <http://link.springer.com/10.1007/BF01349680>.
- [10] S. Adachi, *Physical Review B* **38**, 12966 (1988), ISSN 01631829.
- [11] P. Moontragoon, R. A. Soref, and Z. Ikonc, *Journal of Applied Physics* **112** (2012), ISSN 00218979.
- [12] P. M. Pearce, C. A. Broderick, M. P. Nielsen, A. D. Johnson, and N. J. Ekins-Daukes, *Phys. Rev. Materials* **6**, 015402 (2022), URL <https://link.aps.org/doi/10.1103/PhysRevMaterials.6.015402>.
- [13] S. Wirths, D. Buca, and S. Mantl, *Progress in Crystal Growth and Characterization of Materials* **62**, 1 (2016), ISSN 09608974, URL <http://dx.doi.org/10.1016/j.pcrysgrow.2015.11.001>.
- [14] M. Bauer, C. Ritter, P. A. Crozier, J. Ren, J. Menendez, G. Wolf, and J. Kouvetakis, *Applied Physics Letters* **83**, 2163 (2003), ISSN 00036951, URL <http://aip.scitation.org/doi/10.1063/1.1606104>.
- [15] R. Soref, J. Kouvetakis, J. Tolle, J. Menendez, and V. D’Costa, *Journal of Materials Research* **22**, 3281 (2007), ISSN 0884-2914, URL http://www.journals.cambridge.org/abstract_{_}S0884291400026807.
- [16] S. Wirths, A. T. Tiedemann, Z. Ikonc, P. Harrison, B. Holländer, T. Stoica, G. Mussler, M. Myronov, J. M. Hartmann, D. Grützmacher, et al., *Applied Physics Letters* **102**, 192103 (2013), ISSN 00036951, URL <http://aip.scitation.org/doi/10.1063/1.4805034>.
- [17] S. Wirths, D. Buca, Z. Ikonc, P. Harrison, A. T. Tiedemann, B. Holländer, T. Stoica, G. Mussler, U. Breuer, J. M. Hartmann, et al., *Thin Solid Films* **557**, 183 (2014), ISSN 00406090.
- [18] S. Wirths, Z. Ikonc, N. von den Driesch, G. Mussler, U. Breuer, A. Tiedemann, P. Bernardy, B. Hollander, T. Stoica, J.-M. Hartmann, et al., *ECS Transactions* **64**, 689 (2014), ISSN 1938-6737, URL <https://iopscience.iop.org/article/10.1149/06406.0689ecsthttps://iopscience.iop.org/article/10.1149/06406.0689ecst/meta>.
- [19] T. Wendav, I. A. Fischer, M. Montanari, M. H. Zoellner, W. Klesse, G. Capellini, N. Von Den Driesch, M. Oehme, D. Buca, K. Busch, et al., *Applied Physics Letters* **108** (2016), ISSN 00036951, URL <http://dx.doi.org/10.1063/1.4953784>.

- [20] I. A. Fischer, A. Berrier, F. Hornung, M. Oehme, P. Zaumseil, G. Capellini, N. von den Driesch, Dan Buca, and J. Schulze, *Semiconductor Science and Technology* **32**, 124004 (2017), ISSN 0268-1242, URL <http://link.aps.org/doi/10.1103/PhysRevB.73.125207><https://link.aps.org/doi/10.1103/PhysRevB.73.125207><http://stacks.iop.org/0268-1242/32/i=12/a=124004?key=crossref.8f9632396129ae512a0111e5cb8b7b62>.
- [21] H. Lin, R. Chen, W. Lu, Y. Huo, T. I. Kamins, and J. S. Harris, *Applied Physics Letters* **100**, 141904 (2012), ISSN 00036951, URL http://apl.aip.org/resource/1/applab/v100/i14/p141908_{%}5Cnfiles/260/Linetal.-2012-StructuralandopticalcharacterizationofSixGe1?{%}5Cnfiles/261/Linetal.-2012-StructuralandopticalcharacterizationofSixGe1?
- [22] V. R. D'Costa, Y. S. Fang, J. Tolle, J. Kouvetakis, and J. Menéndez, *Thin Solid Films* **518**, 2531 (2010), ISSN 00406090.
- [23] O. Madelung, U. Rössler, and M. Schulz, eds., *Group IV Elements, IV-IV and III-V Compounds. Part b - Electronic, Transport, Optical and Other Properties*, vol. b of *Landolt-Börnstein - Group III Condensed Matter* (Springer-Verlag, Berlin/Heidelberg, 2002), ISBN 3-540-42876-3, URL <http://materials.springer.com/bp/docs/978-3-540-31356-4>.
- [24] B. Johs, C. Herzinger, J. Dinan, A. Cornfeld, and J. Benson, *Thin Solid Films* **313**, 137 (1998), ISSN 00406090.
- [25] J.A. Woollam Co., Tech. Rep. (2012).
- [26] S. Adachi, in *Physical Properties of III-V Semiconductor Compounds* (Wiley-VCH Verlag GmbH & Co. KGaA, Weinheim, FRG, 2005), vol. 783, pp. 135–192, ISBN 0471573299, URL <http://doi.wiley.com/10.1002/352760281X.ch8>.
- [27] J. W. Fleming, *Applied Optics* **23**, 4486 (1984), ISSN 0003-6935, URL <https://www.osapublishing.org/abstract.cfm?URI=ao-23-24-4486>.
- [28] V. R. D'Costa, C. S. Cook, A. G. Birdwell, C. L. Littler, M. Canonico, S. Zollner, J. Kouvetakis, and J. Menéndez, *Physical Review B* **73**, 125207 (2006), ISSN 1098-0121, URL <https://link.aps.org/doi/10.1103/PhysRevB.73.125207>.
- [29] See Supplemental Material at [URL] for (1) details of the critical point fitting method used to fit the differentiated SE data; (2) discussion of the expected critical thickness of the $\text{Si}_x\text{Ge}_{1-x-y}\text{Sn}_y$ epitaxial layers on Ge and GaAs substrates; (3) ellipsometry data for the Set A samples, comparison of the parametric model and point-by-point fits, and the fit parameters obtained for all samples and (4) XRD reciprocal space maps.
- [30] V. R. D'Costa, C. S. Cook, J. Menéndez, J. Tolle, J. Kouvetakis, and S. Zollner, *Solid State Communications* **138**, 309 (2006), ISSN 00381098.
- [31] R. People and J. C. Bean, *Applied Physics Letters* **47**, 322 (1985), ISSN 0003-6951, URL <http://aip.scitation.org/doi/10.1063/1.96206>.
- [32] P. M. Pearce, *Data for "Compositional dependence of direct transition energies in SiGeSn alloys lattice-matched to Ge/GaAs"* (2022), URL <https://doi.org/10.5281/zenodo.6342594>.
- [33] C. Xu, C. L. Senaratne, J. Kouvetakis, and J. Menéndez, *Solid State Electronics* **110**, 76 (2015), ISSN 0038-1101, URL <http://dx.doi.org/10.1016/j.sse.2015.01.015>.
- [34] P. Aella, C. Cook, J. Tolle, S. Zollner, A. V. G. Chizmeshya, and J. Kouvetakis, *Applied Physics Letters* **84**, 888 (2004), ISSN 0003-6951, URL <http://aip.scitation.org/doi/10.1063/1.1645324>.
- [35] J. Matthews and A. Blakeslee, *Journal of Crystal Growth* **27**, 118 (1974), ISSN 00220248, URL <http://linkinghub.elsevier.com/retrieve/pii/S0022024874800552>.
- [36] L. Vina, S. Logothetidis, and M. Cardona, *Physical Review B* **30**, 1979 (1984), ISSN 01631829.
- [37] J. D. Gallagher, C. L. Senaratne, J. Kouvetakis, and J. Menéndez, *Applied Physics Letters* **105**, 1 (2014), ISSN 00036951.
- [38] T. V. Elzhov, K. M. Mullen, A.-N. Spiess, and B. Bolker, *minpack.lm: R Interface to the Levenberg-Marquardt Nonlinear Least-Squares Algorithm Found in MINPACK, Plus Support for Bounds* (2016), URL <https://cran.r-project.org/package=minpack.lm>.
- [39] Depolarization occurs when the bulk of the sample becomes transparent, and thus the incident polarized light is able to travel through the sample, reflecting at the back surface and returning to the front of the sample, where it can be collected by the detector. As this light has travelled a comparatively large distance through the sample (hundreds of microns compared to hundreds of nanometres), it is no longer coherent with the rest of the signal and causes depolarization of the measured signal.
- [40] The Poisson ratio describes the out-of-plane distortion for in-plane strain.